Correlated insulating states at fractional fillings of moiré superlattices

https://doi.org/10.1038/s41586-020-2868-6

Received: 28 April 2020

Accepted: 3 September 2020

Published online: 11 November 2020

Check for updates

Yang Xu[1]✉, Song Liu[2], Daniel A. Rhodes[2], Kenji Watanabe[3], Takashi Taniguchi[3], James Hone[2], Veit Elser[4]✉, Kin Fai Mak[1,4,5]✉ & Jie Shan[1,4,5]✉

Quantum particles on a lattice with competing long-range interactions are ubiquitous in physics; transition metal oxides[1,2], layered molecular crystals[3] and trapped-ion arrays[4] are a few examples. In the strongly interacting regime, these systems often show a rich variety of quantum many-body ground states that challenge theory[2]. The emergence of transition metal dichalcogenide moiré superlattices provides a highly controllable platform in which to study long-range electronic correlations[5–12]. Here we report an observation of nearly two dozen correlated insulating states at fractional fillings of tungsten diselenide/tungsten disulfide moiré superlattices. This finding is enabled by a new optical sensing technique that is based on the sensitivity to the dielectric environment of the exciton excited states in a single-layer semiconductor of tungsten diselenide. The cascade of insulating states shows an energy ordering that is nearly symmetric about a filling factor of half a particle per superlattice site. We propose a series of charge-ordered states at commensurate filling fractions that range from generalized Wigner crystals[7] to charge density waves. Our study lays the groundwork for using moiré superlattices to simulate a wealth of quantum many-body problems that are described by the two-dimensional extended Hubbard model[3,13,14] or spin models with long-range charge–charge and exchange interactions[15,16].

Moiré superlattices are formed by stacking two identical lattices with a small twist angle or two lattices with a small period mismatch. The flat electronic minibands afforded by moiré superlattices have led to a plethora of emergent phenomena. Graphene moiré systems show superconductivity, correlated insulating states and topological phases[17–26]. With substantially stronger correlation, transition metal dichalcogenide (TMD) moiré superlattices manifest a Mott insulator state at one hole per superlattice site and generalized Wigner crystallization of holes at filling factors of 1/3 and 2/3 (refs. [6,7]). The latter indicates the importance of an intersite interaction (that is, long-range, V) as well as an on-site Coulomb repulsion interaction (U) when compared with the kinetic lattice hopping (t). As a result of the strong long-range interactions, a rich phase diagram of correlated states is foreseen and calls for experimental and theoretical investigations.

Here we unveil an abundance of correlated insulating states at fractional fillings of tungsten diselenide/tungsten disulfide (WSe_2/WS_2) moiré superlattices. They arise from charge ordering in the underlying superlattice and show a broad range of energy scales ranging from much greater than t to about the same order as t. In the limit of $U \gg V$ and t as in WSe_2/WS_2 moiré superlattices, the system with less than one particle per site is effectively described by the t–V model[3,13,14]. Our results show that the excitation energy of the charge-ordered states is widely variable with respect to t, and the nature of these states is much richer than the generalized Wigner crystals. This work demonstrates that TMD moiré superlattices can be used as a quantum simulator of problems described by the t–V and related models, potentially including the metal–insulator transition, unconventional superconductivity and quantum magnetism[1,2].

Dielectric sensing with excitons

The finding is made possible by a new local dielectric sensor in the form of a monolayer TMD semiconductor such as WSe_2. The material interacts strongly with light and forms exciton (bound electron–hole pair) states similar to the Rydberg states of a two-dimensional (2D) hydrogen atom[27]. In particular, the exciton excited states (2s, 3s and so on) have Bohr radii many times the monolayer thickness and are sensitive to the dielectric environment[28]. By placing the sensor in close proximity, we probe the insulating states in TMD moiré superlattices optically by measuring the resonance energy and oscillator strength of the exciton excited states in the sensor. The technique circumvents the large TMD–metal contact resistance (caused by the large TMD bandgap) that challenges direct electrical transport measurements in TMD moiré superlattices, particularly at low carrier densities and low temperatures.

We first demonstrate the technique by probing a WS_2 monolayer that can be gate-tuned from an insulating (incompressible) to a metallic (compressible) state. Figure 1a shows the device structure. A WSe_2 sensor is placed about 1 nm below the sample with a hexagonal boron nitride (hBN) spacer. The spacer thickness is chosen to quench electronic

[1]School of Applied and Engineering Physics, Cornell University, Ithaca, NY, USA. [2]Department of Mechanical Engineering, Columbia University, New York, NY, USA. [3]National Institute for Materials Science, Tsukuba, Japan. [4]Laboratory of Atomic and Solid State Physics, Cornell University, Ithaca, NY, USA. [5]Kavli Institute at Cornell for Nanoscale Science, Ithaca, NY, USA. ✉e-mail: yx542@cornell.edu; ve10@cornell.edu; kinfai.mak@cornell.edu; jie.shan@cornell.edu

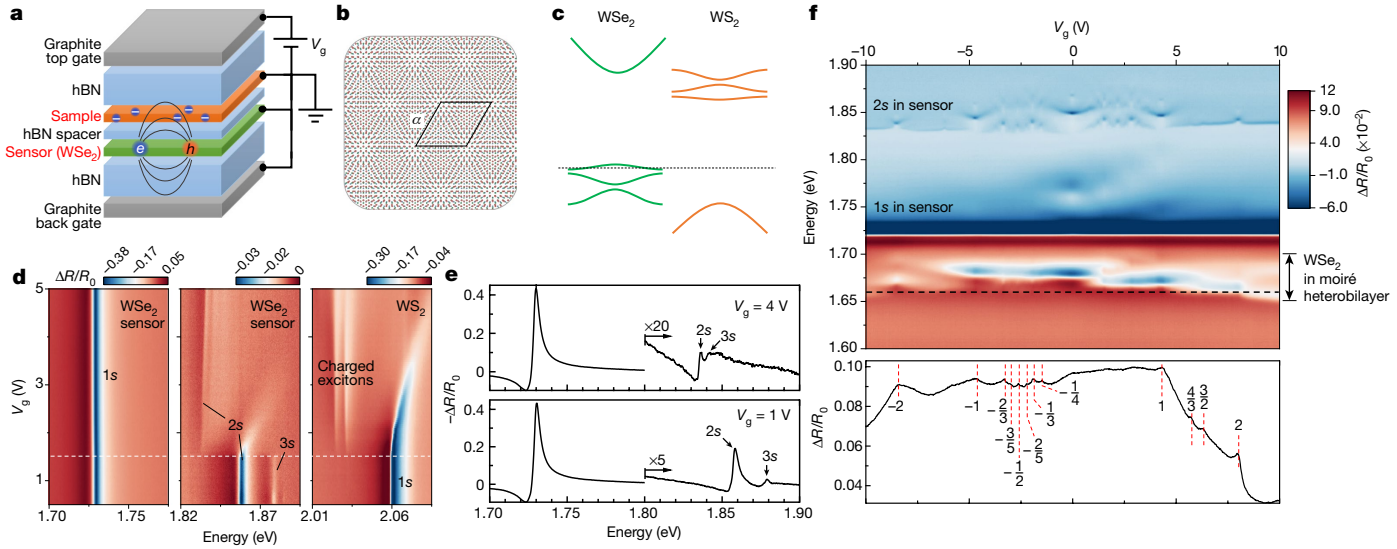

Fig. 1 | Optical sensing of charge gaps using a van der Waals heterostructure platform. a, Schematic of the device structure and electric circuitry. The bound electron–hole pair (exciton) with its electric-field lines beyond the sensor layer probes the charge gap in the sample controlled by electrostatic gating. **b**, Moiré superlattice of period $a \approx 8$ nm formed by angle-aligned WSe_2/WS_2 bilayers. Orange and green (blue) circles denote W and Se (S) atoms, respectively. **c**, Schematic band diagram of WSe_2/WS_2 moiré heterostructures. The chemical potential (dashed line) can be gate-tuned across the heterostructure bandgap. **d**, Gate-dependent reflection contrast ($\Delta R/R_0$) spectrum of the control device with a WS_2 monolayer as the sample at 1.6 K. The three panels (from left to right) show the 1*s* exciton and 2*s* (3*s*) exciton in the sensor, and the 1*s* exciton in the sample, respectively. The sample is electron-doped above $V_g = 1.5$ V (horizontal dashed line). **e**, Two linecuts of **c** at $V_g = 4$ V (top) and $V_g = 1$ V (bottom). The spectra above 1.8 eV are multiplied by a factor of 20 and 5, respectively. **f**, Gate-dependent reflection contrast spectrum of the main device with a WSe_2/WS_2 moiré superlattice as sample at 1.6 K (top) and a line-cut (bottom) at 1.66 eV (black dashed line). The red dashed lines mark the correlated insulating states from Fig. 2 that can potentially be identified from the reflection contrast enhancement of the moiré excitons.

coupling between the sensor and the sample while maintaining their close proximity for high detection sensitivity. The entire structure is encapsulated in roughly 40-nm hBN with a few-layer graphite electrode on both sides. A positive gate voltage V_g is applied between the top gate electrode and the sample to inject electrons into the sample. The sensor remains charge neutral for the gate range shown. (See Methods for details on the device fabrication and optical measurements.)

Figure 1d shows the reflection contrast spectrum of the control device as a function of V_g at 1.6 K. The prominent features in the three panels from left to right correspond to the 1*s* and 2*s* (and 3*s*) excitons in WSe_2 and the 1*s* exciton in WS_2, respectively[27]. For $V_g \gtrsim 1.5$ V (white dashed line), the 1*s* exciton in WS_2 turns into an attractive polaron at a lower energy (also referred to as charged excitons) that becomes stronger with doping and a repulsive polaron that blueshifts and weakens with doping[29]. This signals charge doping into WS_2. At high doping densities, the attractive polaron merges into the band-to-band transitions and the repulsive polaron disappears. Correspondingly, in the sensor, the 1*s* exciton shows negligible changes. However, the behaviour of the 2*s* exciton mirrors that of the 1*s* exciton in the sample. The 3*s* exciton also becomes much weaker.

The observed response of excitons in the sensor to charge doping in the sample can be explained by renormalization of the exciton binding energies and the quasiparticle bandgap by screening of the Coulomb interactions[28,30]. For the 1*s* exciton, the two contributions nearly cancel each other and the resonance energy remains unaffected[30]. The 2*s* state emerges as a sensitive probe of the insulating/metallic state of the sample. For instance, when the undoped WS_2 sample becomes moderately doped in Fig. 1e, the 2*s* exciton redshifts by about 25 meV and its oscillator strength decreases by about 20 times (see Methods for more detail on the sensing mechanism).

Correlated insulating states

We now apply the exciton probe to examine the insulating states in TMD moiré superlattices. We replace the WS_2 monolayer in the control experiment with an angle-aligned WSe_2/WS_2 bilayer, which forms a moiré superlattice with period $a \approx 8$ nm (ref. [31]; Fig. 1b). The WSe_2/WS_2 moiré superlattice has a type-II band alignment (Fig. 1c): positive V_g values inject electrons into WS_2 and negative V_g values inject holes into WSe_2. The moiré potential also lowers the optical gap of the WSe_2 layer compared with the WSe_2 sensor by about 50 meV. This allows us to unambiguously distinguish the optical response of these two different WSe_2 layers.

Figure 1f is the reflection contrast spectrum of the device as a function of V_g at 1.6 K. The features below 1.7 eV are the fundamental moiré excitons in the WSe_2 layer of the superlattice[6,31–34]. They show semi-periodic modulations both in energy and reflection contrast at every half filling of the moiré miniband[6] or integer filling of the superlattice site as each miniband is doubly degenerate from the coupled spin–valley degree of freedom[8]. The lower panel is a line-cut plot of the reflection contrast at 1.66 eV. It shows enhancements at multiple fillings on a broad background, which could be related to the correlated insulating states as we investigate below. The complicated many-body interaction of the moiré excitons with the strongly correlated electron system, however, makes the direct interpretation of the optical response challenging. The strong feature centred at 1.725 eV is the 1*s* exciton of the sensor. Similar to the control experiment, it is doping independent, demonstrating that the sensor remains charge neutral all the time. The 2*s* exciton of the sensor (near 1.84 eV) shows remarkable doping dependences. (Extended Data Fig. 7 compares spectra with and without the sensor.)

We focus on the gate or filling dependence of the 2*s* exciton in Fig. 2a. The filling factor ν is initially determined from the ratio of the doping density (evaluated from V_g and the gate capacitance) to the superlattice density (evaluated from the lattice constants and the twist angle between the layers). We use a positive (negative) filling factor ν for electron (hole) fillings. The gate dependence shows a series of resonance blueshifts, accompanied by an enhancement in reflection contrast. Higher-lying resonances with much smaller oscillator strengths are also observable. They probably arise from the sample-induced moiré

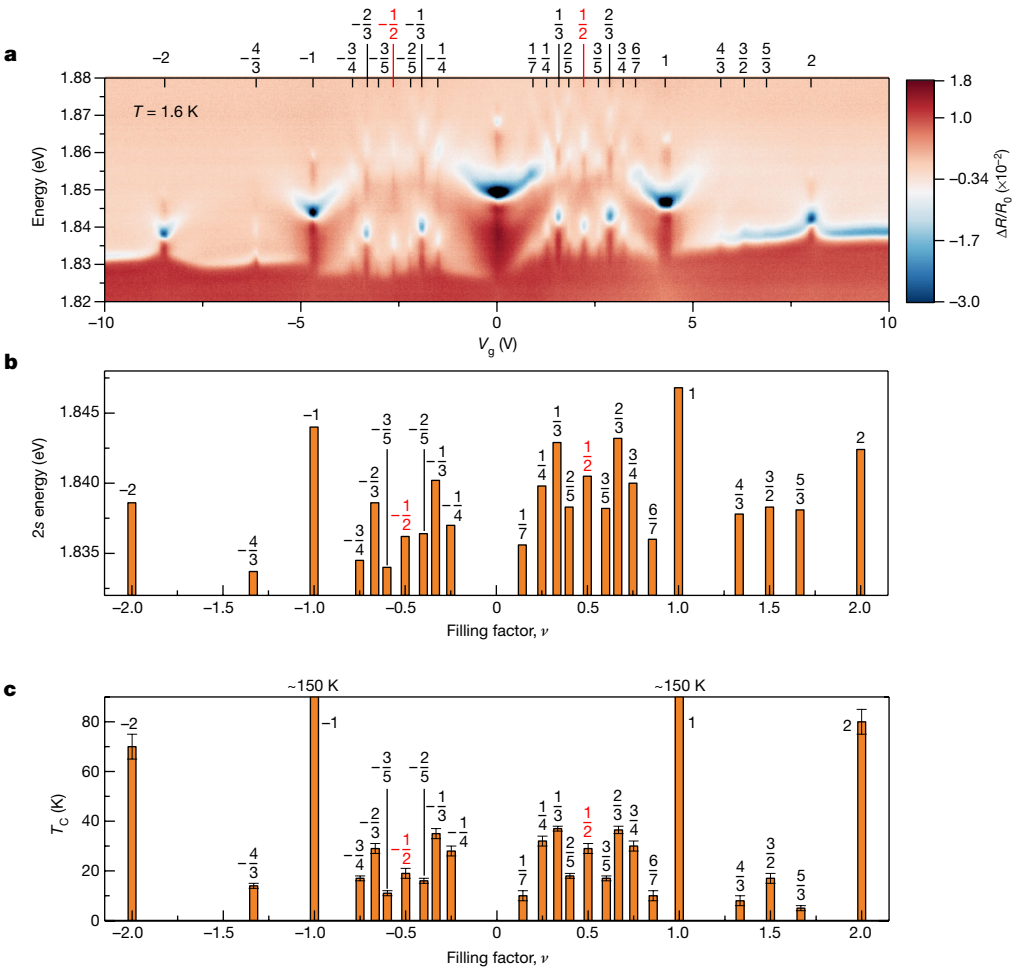

Fig. 2 | An abundance of insulating states and their energy ordering in a WSe_2/WS_2 moiré heterostructure. a, Detail of Fig. 1f focusing on the 2*s* exciton in the sensor. An abundance of insulating states is revealed by blueshifts of the 2*s* exciton resonance, accompanied by an enhancement in the spectral weight. The top axis shows the proposed filling factor for the insulating states. **b**, **c**, The 2*s* exciton resonance energy (**b**) and the critical temperature T_C (**c**) for all of the observed insulating states. A uniform width of about 0.05 is chosen for all of the states for clarity. It is comparable to the average FWHM of the states. The vertical error bars in **c** are standard deviations estimated from Fig. 3. For $|\nu|<1$, the fractional-filling states are symmetric about $|\nu|=1/2$ (marked in red); the energy (T_C) of these states is approximately symmetric about $|\nu|=1/2$, particularly, on the electron side.

bands in the sensor and will not be focused on here. The emergence of the enhanced 2*s* exciton indicates reduced screening and opening of a charge gap in the sample. The strongest 2*s* exciton is observed around 0 V when the sample is charge neutral. The bandgap of the superlattice is by far the largest energy gap in the system. The next few fillings in descending order of the 2*s* exciton strength are $|\nu|=1$, $|\nu|=2$, $|\nu|=1/3$ and $|\nu|=2/3$. These states have been recently reported in hole-doped WSe_2/WS_2 moiré superlattices with the same energy ordering[6,7]. They correspond to a Mott insulator ($\nu=1$), moiré band insulator ($\nu=2$) and generalized Wigner crystals ($\nu=1/3$ and $\nu=2/3$). Our result shows that these strong insulating states occur on both electron-filled and hole-filled superlattices, and there are many weaker insulating states, particularly, at fractional fillings.

We refine the gate voltage–filling factor conversion by using the established insulating states as landmarks and assuming a linear dependence for the electron and hole side independently (Extended Data Fig. 2). The two conversion factors are practically identical. The filling factor of the remaining insulating states is determined from the measured V_g as the closest rational number with a small denominator (Methods). We plot the 2*s* exciton resonance energy for all observed insulating states with $\nu\neq0$ in Fig. 2b. These states have been observed at different locations of the device, and the majority of them also in a different device (Extended Data Figs. 3, 4).

Energy ordering and critical temperature

We determine the energy of each insulating state more quantitatively by performing a temperature-dependence study (Fig. 3a). On heating, the insulating states disappear one by one following a sequence that is largely consistent with the ordering inferred from the 2*s* resonance energy. We track the monotonic decrease of the 2*s* spectral weight with temperature (see an example in Extended Data Fig. 5). For each state, we estimate the critical temperature T_C from the value at which the spectral weight drops to about 10% of its maximum. Figure 3b–f illustrates several examples with $\nu=1/2$, $\nu=2/5$, $\nu=1/3$, $\nu=1/4$, $\nu=1/7$ and their conjugate states at $1-\nu$ with the occupied and empty sites switched. The behaviour of the $1-\nu$ state is nearly identical to that of the ν state. Figure 2c summarizes T_C for all states. The observed 70 K for $\nu=-2$ and 150 K for $\nu=-1$ are in good agreement with earlier electrical transport measurements[6] (see Extended Data Fig. 8 for dependence in the high-temperature range). Here T_C characterizes the bandgap size for the single-particle moiré band insulator ($|\nu|=2$) and the thermodynamic phase transition temperature for the other states. Similar analysis can be performed using the 2*s* resonance energy, but it is less sensitive to temperature than the spectral weight.

The ordering of the T_C values of the insulating states (Fig. 2c) is fully consistent with the ordering of the 2*s* resonance energies (Fig. 2b).

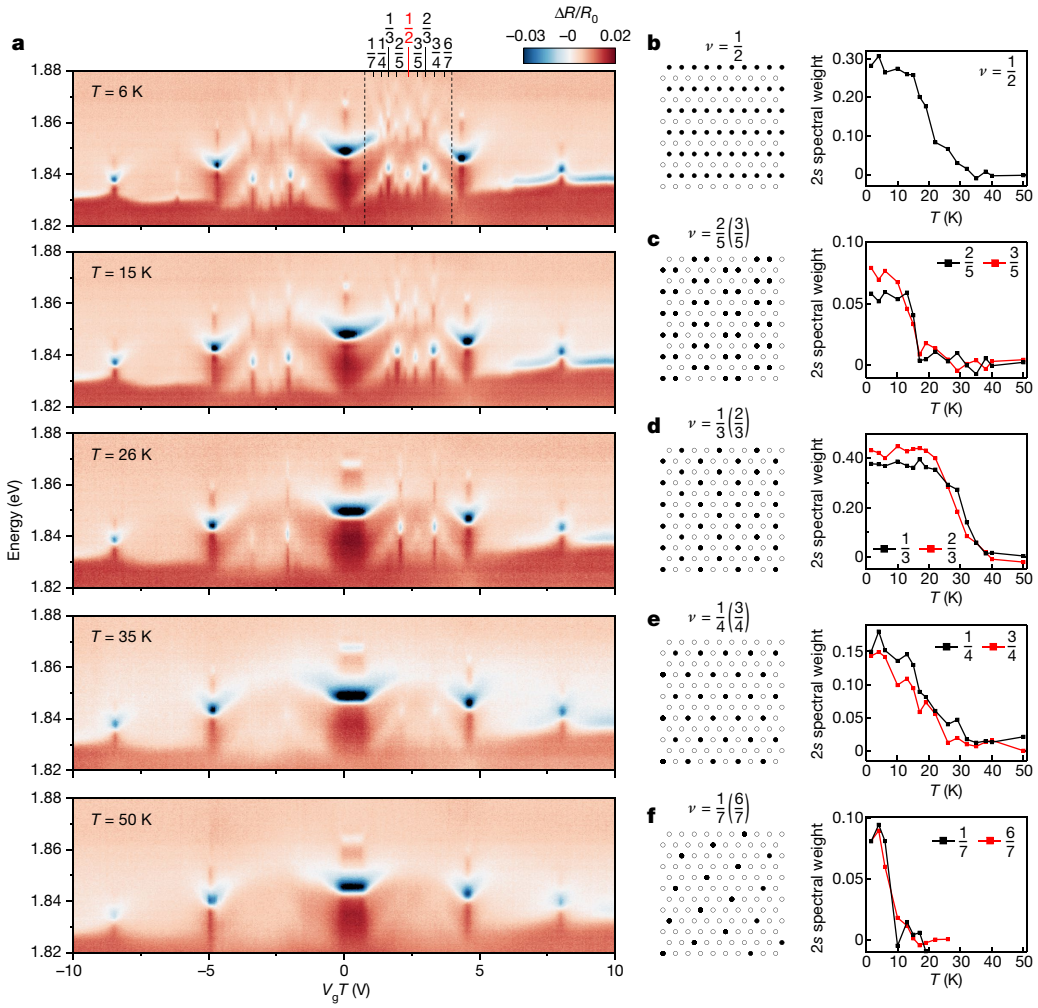

Fig. 3 | Temperature dependence of the correlated insulating states. **a**, Same as Fig. 2a at elevated temperatures (from top to bottom, 6 K, 15 K, 26 K, 35 K and 50 K). With increasing temperature, the correlated insulating states disappear one by one. **b**–**f**, Right: temperature dependence of the 2*s* exciton spectral weight for states ν (1/2 (**b**), 2/5 (**c**), 1/3 (**d**), 1/4 (**e**) and 1/7 (**f**); black symbols) and $1-\nu$ (1/2 (**b**), 3/5 (**c**), 2/3 (**d**), 3/4 (**e**) and 6/7 (**f**); red symbols). The lines are guides to the eye. Left: proposed charge-order configuration at zero temperature on the underlying hexagonal moiré superlattice. Filled and unfilled circles denote occupied and empty sites for state ν, respectively. For state $1-\nu$, the notation of the occupied and empty sites is switched.

The electron and hole sides show almost identical correlated insulating states with similar energy scales, suggesting that the same correlation effect is in play. However, the interaction effect is slightly stronger on the electron side: the states generally have higher T_C values and a few more states are discernible. In addition, for each side, the states at $\nu<1$ generally have higher T_C values than the states at $\nu>1$. Furthermore, the states at $\nu<1$ appear symmetrically about $\nu=1/2$ with comparable T_C values for states ν and $1-\nu$.

In Fig. 3b–f, we propose the electron configurations on the underlying hexagonal superlattice for states at $\nu<1$, including $\nu=1/2$, $\nu=2/5$, $\nu=1/3$, $\nu=1/4$ and $\nu=1/7$. The viability of the configurations was checked, and the charge-ordering temperatures were determined, by performing a classical Monte Carlo simulation with a repulsive Coulomb interaction parameterized by a dielectric constant ε and gate spacing $d/2$ (Methods). Using $d/2=40$ nm, similar to the value in the experiment, we find that the model with $\varepsilon=3.9$ best describes the highest experimental T_C, that of the $\nu=1/3$ state. This value is consistent with the dielectric constant of hBN (3.0 out-of-plane and 6.9 in-plane, $\sqrt{3.0\times6.9}\approx4.5$). That the experimental T_C values of the other states do not all align with the model predictions (Extended Data Table 1) we see as evidence that quantum effects cannot be neglected to properly model the system. In the classical model, the conjugate states ν and $1-\nu$ share the same T_C. Intriguingly, Fig. 3b, c shows that the $\nu=1/2$ and $\nu=2/5$ (3/5) states have a broken rotational symmetry and are stripe phases. Future experiments are required to verify this.

Quantum effects

We briefly discuss the role of quantum fluctuations. In the limit of $t=0$, all the insulating states at fractional fillings are generalized Wigner crystals that are described by the configurations shown in Fig. 3b–f. With increasing t, quantum fluctuations can induce charge leakage into the empty sites and turn the Wigner crystals into charge density waves (CDWs) with reduced spatial modulations in charge density. When t becomes comparable to or even larger than the excitation energy of these states, the charge-ordered states melt into metallic states[1]. In WSe_2/WS_2 moiré superlattices, the parameter t is estimated to be about 1 meV (ref. [8]). If we assume the excitation energy is on the order of T_C, we expect $\nu=1/4$, $\nu=1/3$, $\nu=1/2$, $\nu=2/3$ and $\nu=3/4$ states on the electron side and $\nu=-1/4$, $\nu=-1/3$ and $\nu=-2/3$ states on the hole side to be close to the generalized Wigner crystal states, and the other states close to the CDWs. In addition, the inclusion of t breaks the symmetry of the energy ordering about $|\nu|=1/2$ (particularly clear on the hole side). The interaction effect is stronger for $|\nu|<1/2$ due to a lower charge density and a larger Coulomb-to-kinetic-energy ratio. The effect of finite t could also explain the observed stronger interaction effects on the

electron side. We speculate that the first conduction moiré miniband has a smaller bandwidth than the first valence moiré miniband.

Finally, we discuss the insulating states at $\upsilon > 1$. The $\upsilon = 4/3$ and $\upsilon = 5/3$ states could be a CDW analogue of the $\upsilon = 1/3$ and $\upsilon = 2/3$ states (the $\upsilon = 1/3$ and $\upsilon = 2/3$ charge configuration plus a completely filled lattice background) or pair density waves if $\upsilon = 1$ is a charge-transfer insulator[35,36]. The interaction effect is reduced substantially, so is the T_C. The $\upsilon = 3/2$ state is a peculiar one. Its T_C is substantially higher than that of the $\upsilon = 4/3$ and $\upsilon = 5/3$ states. This is therefore unlikely a CDW analogue of the $\upsilon = 1/2$ state. Interestingly, this filling coincides with a van Hove singularity in the density of states of the superlattice[8]. Exotic magnetically ordered states[37,38] and superconductivity[39] have been predicted at van Hove singularities. Whether the $\upsilon = 3/2$ state is of exotic origin deserves further investigations.

Online content

Any methods, additional references, Nature Research reporting summaries, source data, extended data, supplementary information, acknowledgements, peer review information; details of author contributions and competing interests; and statements of data and code availability are available at https://doi.org/10.1038/s41586-020-2868-6.

1. Imada, M., Fujimori, A. & Tokura, Y. Metal–insulator transitions. *Rev. Mod. Phys*. **70**, 1039–1263 (1998).
2. Dagotto, E. Complexity in strongly correlated electronic systems. *Science* **309**, 257–262 (2005).
3. Hotta, C. Theories on frustrated electrons in two-dimensional organic solids. *Crystals* **2**, 1155–1200 (2012).
4. Lahaye, T., Menotti, C., Santos, L., Lewenstein, M. & Pfau, T. The physics of dipolar bosonic quantum gases. *Rep. Prog. Phys*. **72**, 126401 (2009).
5. Zhu, Q., Tu, M. W. Y., Tong, Q. & Yao, W. Gate tuning from exciton superfluid to quantum anomalous Hall in van der Waals heterobilayer. *Sci. Adv*. **5**, eaau6120 (2019).
6. Tang, Y. et al. Simulation of Hubbard model physics in WSe_2/WS_2 moiré superlattices. *Nature* **579**, 353–358 (2020).
7. Regan, E. C. et al. Mott and generalized Wigner crystal states in WSe_2/WS_2 moiré superlattices. *Nature* **579**, 359–363 (2020).
8. Wu, F., Lovorn, T., Tutuc, E. & Macdonald, A. H. Hubbard model physics in transition metal dichalcogenide moiré bands. *Phys. Rev. Lett*. **121**, 026402 (2018).
9. Wu, F., Lovorn, T., Tutuc, E., Martin, I. & Macdonald, A. H. Topological insulators in twisted transition metal dichalcogenide homobilayers. *Phys. Rev. Lett*. **122**, 086402 (2019).
10. Shimazaki, Y. et al. Strongly correlated electrons and hybrid excitons in a moiré heterostructure. *Nature* **580**, 472–477 (2020).
11. Wang, L. et al. Correlated electronic phases in twisted bilayer transition metal dichalcogenides. *Nat. Mater*. **19**, 861–866 (2020).
12. Zhang, Z. et al. Flat bands in twisted bilayer transition metal dichalcogenides. *Nat. Phys*. https://doi.org/10.1038/s41567-020-0958-x (2020).
13. Pietig, R., Bulla, R. & Blawid, S. Reentrant charge order transition in the extended Hubbard model. *Phys. Rev. Lett*. **82**, 4046–4049 (1999).
14. Tocchio, L. F., Gros, C., Zhang, X. F. & Eggert, S. Phase diagram of the triangular extended Hubbard model. *Phys. Rev. Lett*. **113**, 246405 (2014).
15. McKenzie, R. H., Merino, J., Marston, J. B. & Sushkov, O. P. Charge ordering and antiferromagnetic exchange in layered molecular crystals of the θ type. *Phys. Rev. B* **64**, 085109 (2001).
16. Porras, D. & Cirac, J. I. Quantum manipulation of trapped ions in two dimensional coulomb crystals. *Phys. Rev. Lett*. **96**, 250501 (2006).
17. Cao, Y. et al. Correlated insulator behaviour at half-filling in magic-angle graphene superlattices. *Nature* **556**, 80–84 (2018).
18. Cao, Y. et al. Unconventional superconductivity in magic-angle graphene superlattices. *Nature* **556**, 43–50 (2018).
19. Sharpe, A. L. et al. Emergent ferromagnetism near three-quarters filling in twisted bilayer graphene. *Science* **365**, 605–608 (2019).
20. Yankowitz, M. et al. Tuning superconductivity in twisted bilayer graphene. *Science* **363**, 1059–1064 (2019).
21. Serlin, M. et al. Intrinsic quantized anomalous Hall effect in a moiré heterostructure. *Science* **367**, 900–903 (2020).
22. Lu, X. et al. Superconductors, orbital magnets and correlated states in magic-angle bilayer graphene. *Nature* **574**, 653–657 (2019).
23. Chen, G. et al. Evidence of a gate-tunable Mott insulator in a trilayer graphene moiré superlattice. *Nat. Phys*. **15**, 237–241 (2019).
24. Chen, G. et al. Signatures of tunable superconductivity in a trilayer graphene moiré superlattice. *Nature* **572**, 215–219 (2019).
25. Chen, G. et al. Tunable correlated Chern insulator and ferromagnetism in a moiré superlattice. *Nature* **579**, 56–61 (2020); correction **581**, E3 (2020).
26. Padhi, B., Setty, C. & Phillips, P. W. Doped twisted bilayer graphene near magic angles: proximity to Wigner crystallization, not Mott insulation. *Nano Lett*. **18**, 6175–6180 (2018).
27. Wang, G. et al. Excitons in atomically thin transition metal dichalcogenides. *Rev. Mod. Phys*. **90**, 021001 (2018).
28. Raja, A. et al. Coulomb engineering of the bandgap and excitons in two-dimensional materials. *Nat. Commun*. **8**, 15251 (2017).
29. Sidler, M. et al. Fermi polaron-polaritons in charge-tunable atomically thin semiconductors. *Nat. Phys*. **13**, 255–261 (2017).
30. Gao, S., Liang, Y., Spataru, C. D. & Yang, L. Dynamical excitonic effects in doped two-dimensional semiconductors. *Nano Lett*. **16**, 5568–5573 (2016).
31. Jin, C. et al. Observation of moiré excitons in WSe_2/WS_2 heterostructure superlattices. *Nature* **567**, 76–80 (2019); correction **569**, E7 (2019).
32. Tran, K. et al. Evidence for moiré excitons in van der Waals heterostructures. *Nature* **567**, 71–75 (2019).
33. Alexeev, E. M. et al. Resonantly hybridized excitons in moiré superlattices in van der Waals heterostructures. *Nature* **567**, 81–86 (2019); correction **572**, E8 (2019).
34. Seyler, K. L. et al. Signatures of moiré-trapped valley excitons in $MoSe_2/WSe_2$ heterobilayers. *Nature* **567**, 66–70 (2019).
35. Zhang, Y., Yuan, N. F. Q. & Fu, L. Moiré quantum chemistry: charge transfer in transition metal dichalcogenide superlattices. Preprint at https://arxiv.org/abs/1910.14061 (2019).
36. Slagle, K. & Fu, L. Charge transfer excitations, pair density waves, and superconductivity in moiré materials. Preprint at https://arxiv.org/abs/2003.13690 (2020).
37. Martin, I. & Batista, C. D. Itinerant electron-driven chiral magnetic ordering and spontaneous quantum hall effect in triangular lattice models. *Phys. Rev. Lett*. **101**, 156402 (2008).
38. Nandkishore, R., Chern, G. W. & Chubukov, A. V. Itinerant half-metal spin-density-wave state on the hexagonal lattice. *Phys. Rev. Lett*. **108**, 227204 (2012).
39. Nandkishore, R., Thomale, R. & Chubukov, A. V. Superconductivity from weak repulsion in hexagonal lattice systems. *Phys. Rev. B* **89**, 144501 (2014).

Methods

Device fabrication and electrostatic gating

The van der Waals heterostructures shown in Fig. 1a are prepared by a layer-by-layer dry-transfer method[40] and released on silicon (Si) substrates with a 100-nm oxide layer. The raw 2D materials, including the WSe_2 and WS_2 monolayers and few-layer graphite and hBN, are first mechanically exfoliated from bulk crystals on Si substrates. Flakes of appropriate size and thickness are selected according to their optical contrast. Monolayer WSe_2 and WS_2 in the moiré superlattice are aligned with a twist angle close to 0°. We employ angle-resolved optical second harmonic generation (details described elsewhere[6,31]) to determine the crystal orientations of the two monolayers and align them accordingly in the stacking process. A thin hBN spacer (typically about 1 nm thick) separates the sample and the WSe_2 sensor to quench direct coupling between them. Few-layer graphite is used as contact and gate electrodes. They are connected to the pre-patterned gold electrodes on the substrate. The gate dielectric material hBN on each side has a typical thickness of 35–40 nm. To tune the charge density in the sample and keep the sensor layer charge neutral, a voltage V_g is applied to the top-gate electrode through a Keithley 2400 source meter while all other layers are grounded.

Optical measurements

The reflection contrast spectroscopy measurements are performed with the devices inside a close-cycle optical cryostat (Attocube, attoDRY2100) with variable-temperature capability (1.6–300 K). A halogen lamp serves as a white light source, the output of which is first collected by a single-mode fibre and collimated by a ×10 objective. The beam is then focused onto the sample by a low-temperature-compatible apochromatic objective with a numerical aperture of 0.8. The beam on the sample has a diameter of about 1 μm and a power below 1 nW. The reflected light from the sample is collected by the same objective and detected by a spectrometer. The reflection contrast ($\Delta R/R_0$) spectrum is obtained by comparing the spectrum of light reflected from the sample (R) and from the substrate right next to the sample (R_0) as $(R-R_0)/R_0$. The measurement sensitivity for $\Delta R/R_0$ is about 0.1%.

Mechanism of sensitivity of 2D excitons to dielectric environment

Excitons in atomically thin TMDs have been actively studied. Dielectric screening of the Coulomb interactions is known to be important to understanding the exciton binding energy and other key properties[27,28]. The problem of an electron and hole in two dimensions with an attractive $1/r$ Coulomb interaction (r denoting the electron–hole separation) can be solved analytically (the 2D hydrogen model). They form excitons and the binding energy of the nth state is given $E_b^{(n)} = \frac{m_r e^4}{2\hbar^2(4\pi\varepsilon\varepsilon_0)^2(n-\frac{1}{2})^2}$. Here ε is the dielectric constant of a uniform dielectric medium, in which the exciton is immersed; ε_0 denotes the vacuum permittivity; m_r is the exciton reduced mass; e is the elementary charge; and $\hbar$ is the reduced Planck constant. However, although the bound electron and hole in monolayer TMDs are confined in two dimensions, the electric-field lines between them exist in three dimensions (Fig. 1a). Screening of the Coulomb interaction is thus distance dependent. The screened Coulomb interaction can be well described by the Keldysh potential[41,42]. It scales as roughly $\ln r$ at short range, and reduces back to about $1/r$ at long range. The screening length for monolayer WSe_2 in vacuum is about 4.5 nm while the Bohr radius of the exciton excited states exceeds 5–6 nm (ref. [42]). The 2D hydrogen model therefore remains a good approximation for exciton exited states. For instance, the 2s exciton binding energy E_b^{2s} can be extracted from the 2s and 3s energy spacing as $E_b^{2s} \approx \frac{25}{16}(E_b^{2s} - E_b^{3s})$ without knowing the location of the quasiparticle continuum[41,43].

We consider our experimental geometry, where the TMD monolayer (sensor) is in close proximity to another 2D layer with a gate-tunable dielectric response. The dielectric response of the medium $\varepsilon(q,E)$ is now a complex function of wavevector (q) and frequency or energy (E). To correctly account for the dynamic screening effect, for a given $\varepsilon(q,E)$ the exciton binding energy needs to be calculated self-consistently with an energy cut-off determined by the exciton binding energy and a wavevector cut-off by the exciton Bohr radius. Furthermore, the finite spatial separation between the sensor and sample layers needs to be appropriately taken into account. It is challenging to find the exact solution for excitons in this problem. Below we consider the limit of small exciton binding energies to obtain a qualitative picture.

In the limit of small exciton binding energies, we use the dielectric function in the static limit $\varepsilon(q)$. Thomas–Fermi screening yields $\varepsilon(q) = \varepsilon_b + \frac{e^2}{\varepsilon_0 t q^2}\frac{\partial n}{\partial \mu}$ for a uniformly screened Coulomb potential by a free electron gas. Here $\frac{\partial n}{\partial \mu}$ is the electronic density of states or compressibility, ε_b is the background dielectric response (from bound charges) and t is the thickness of the 2D layer. Combining this result with the 2D hydrogen model ($E_b^{(n)} \propto 1/\varepsilon^2$), we expect renormalization in the exciton binding energy in the sensor to be dependent on $\frac{\partial n}{\partial \mu}$ in the sample. Larger density of states would give rise to an enhanced dielectric function and reduced exciton binding energies. This qualitative picture is consistent with our control experiment at higher doping densities (Fig. 1d). The 2s exciton resonance energy shows a stepwise redshift (reduced binding energy) when the sample layer (monolayer WS_2) is gate-tuned from an insulating (incompressible) to a metallic (compressible) state. The 2s exciton energy remains constant with further doping as $\frac{\partial n}{\partial \mu}$ is a constant for 2D massive particles.

The situation becomes more complex at low doping levels in the sample when the electron–electron spacing is comparable to or larger than the 2s exciton Bohr radius in the sensor. In this regime, the long-wavelength (Thomas–Fermi) approximation is expected to break down. In the experiment (Fig. 1d, Extended Data Fig. 1), both an abruptly redshifted feature and a continuously blueshifted feature coexist. They probably correspond to the attractive and repulsive interlayer polarons, respectively, which are formed when the 2s exciton in the sensor dynamically polarizes the electron sea in the sample layer[44]. Similar to the intralayer polarons in WS_2, the oscillator strength of the repulsive interlayer polaron quickly diminishes with doping and the attractive interlayer polaron merges into the band-to-band transitions at high doping levels. A quantitative understanding in this regime, however, requires further investigations.

Assignment of the filling factor for the insulating states

The filling factor υ is defined as the number of electrons or holes per moiré superlattice site. We first estimate υ from the ratio of the charge density to the superlattice density[6]. The charge density acquired from electrostatic gating is given by the capacitance of the device and applied gate voltage V_g. The capacitance is dominated by the geometrical capacitance of the gate and hence is approximately a constant. It is evaluated to be about 76 nF cm^{-2} from the thickness (about 35 nm) and out-of-plane dielectric constant (about 3) of the hBN gate dielectric[45]. The superlattice density is evaluated to be 1.9×10^{12} cm^{-2} from the moiré period for a nearly 0°-aligned WSe_2/WS_2 bilayer. The uncertainty in υ is of the order of 10%.

To better determine υ, we use the established insulating states $\upsilon = 1$, $\upsilon = 2$, $\upsilon = 1/3$ and $\upsilon = 2/3$ as landmarks and extract the conversion factor from gate voltage to filling factor for electron and hole doping independently. This removes the difficulty with identifying the band edges (that is, the value of V_g for $\upsilon = 0$) and allows a range of V_g for the Fermi level to be inside the heterostructure bandgap. We first determine V_g for all of the insulating states. For states that are clearly identifiable, we obtain their peak position and the full-width at half-maximum (FWHM) by performing a Lorentzian fit to the reflection contrast at a fixed photon energy (the 2s resonance energy for the given state) as a function of V_g. Extended Data Fig. 5a, b shows examples of the analysis for states

$\upsilon = -1/3$ and $\upsilon = -2/3$. For less well-developed states ($1 < \upsilon < 2$), we estimate the peak position and peak width from the first derivative with respect to energy of the reflection contrast contour plot (see Extended Data Fig. 6 for an example at 1.6 K).

We perform linear fits using the V_g values for states $\upsilon = 1$, $\upsilon = 2$, $\upsilon = 1/3$ and $\upsilon = 2/3$ on the electron and hole side independently. The slopes are basically identical. They correspond to about 0.25 filling per volt. The value does not depend on temperature strongly up to 50 K. The filling factor of the remaining insulating states is determined from the corresponding gate voltage and the conversion factor. We assign each to the closest rational number with a small denominator as it usually has lower energy. For instance, state $\upsilon = 1/4$ is very close to 6/25, 7/30 and so on, but is assigned to 1/4 as its denominator is the smallest. In addition, at low doping levels, we observe a nonlinear gating effect, particularly for hole doping presumably because of the non-ideal electrical contacts to the TMD superlattices. We correct this effect by using the established symmetry between states υ and $1 - \upsilon$. For instance, the −1/4 state is assigned by its resemblance in 2*s* exciton energy and oscillator strength as well as T_C to the −3/4 state, whose assignment does not suffer from the nonlinear gating complication.

Extended Data Fig. 2 summarizes the assigned υ and the corresponding V_g for all observed insulating states. The horizontal bar for each state denotes its FWHM in V_g, or equivalently, doping, not the uncertainty in determining the peak position. The uncertainty for the peak position from the Lorentzian fit is substantially smaller.

Effect of the sensor orientation and location

We have examined two different WSe_2/WS_2 bilayer devices in this study. The one presented in Extended Data Fig. 4 differs from the one presented in the main text in several ways. It has: (1) a hBN spacer of about 0.65 nm, compared with 1.3 nm in the main device; (2) an angle-misaligned (about 25°) sensor to the moiré superlattice, compared with an angle-aligned sensor to the moiré superlattice in the main device; and (3) the sensor on the WS_2 side rather than the WSe_2 side of the moiré superlattice as in the main device. No clear dependence on the sensor orientation is observed. The absence of sensor twist angle dependence can be understood by the short-range nature of the moiré potential. In general, the moiré potential arises from spatially dependent interlayer hopping between two layers in direct contact with each other[6,7,11,17–25]. The interlayer hopping is expected to decay exponentially with layer separation on the atomic length scale. In the presence of a hBN spacer of about 1 nm, negligible moiré potential is expected on the sensor.

A clear dependence of the detection sensitivity on the spacer thickness is observed. The spectral shift of the 2*s* resonance between a compressible and incompressible state is larger in the device with a thinner spacer as more efficient screening is expected. For instance, the 2*s* resonance energy shift between the $\upsilon = 1$ state and the state immediately above $\upsilon = 1$ is over 20 meV in Extended Data Fig. 4, in contrast to about 12 meV in the main device. Given the 2*s* exciton Bohr radius in monolayer WSe_2 to be about 5 nm, we expect a substantial drop in the sensor sensitivity when the hBN spacer thickness becomes comparable to 5 nm. Finally, we note that the detection sensitivity for electron and hole doping of the WSe_2/WS_2 bilayer can be different depending on which moiré layer (WSe_2 or WS_2) is adjacent to the sensor. The one that is closer to the sensor is expected to have a better detection sensitivity.

Effects of sample inhomogeneity

Extended Data Fig. 3 shows the results from five additional regions of the main device. The data quality varies from location to location. For instance, the level of inhomogeneities at region P4 is higher than that at the other regions. Many of the weaker correlated states are smeared out at P4 while almost all of the states remain identifiable at P1. This can also be seen in the larger filling linewidth for each of the correlated states in P4. The sample inhomogeneity can arise from twist angle disorder and/or charge impurities in the moiré superlattice. However, the effect of twist angle disorder in TMD heterobilayers with a large lattice mismatch is not expected to be important in our devices. Owing to a large lattice mismatch (4%) between WSe_2 and WS_2, the moiré period and density are relatively insensitive to the twist angle in nearly angle-aligned structures. This is in marked contrast to homobilayers or heterobilayers with a small lattice mismatch. As the observed correlated states display systematic ordering in energy scales and near symmetry about $\upsilon = 1/2$ in both the 2*s* resonance energy and reflection contrast, they are distinct states rather than the same state from different regions due to sample inhomogeneities.

Modelling

In the classical model, we keep only the potential energy terms in the extended Hubbard Hamiltonian:

$$\mathcal{H}(n) = \frac{1}{2}\sum_i \sum_{j\neq i} V(r_{ij}) n_i n_j. \quad (1)$$

Here $n_i \in \{0, 1\}$ are the occupations of the sites i of the hexagonal moiré superlattice, r_{ij} is the distance between sites i and j, and we use the potential model where the moiré heterobilayer is adjacent to conducting sheets on both sides with spacing $d/2$:

$$V(r) = \frac{e^2}{4\pi\varepsilon\varepsilon_0} \sum_{k=-\infty}^{\infty} \frac{(-1)^k}{\sqrt{r^2 + (kd)^2}} \quad (2)$$

We state all lengths in the model in units of the moiré lattice constant a and our unit of energy is $e^2/(4\pi\varepsilon\varepsilon_0 a)$. The potential $V(r)$ decays exponentially with r and the sum $\sum_{j\neq i} V(r_{ij})$ converges to a value independent of the site i. This implies, at fixed filling

$$\mathcal{H}(n) = \mathcal{H}(1 - n) + \text{constant}. \quad (3)$$

Consequently, any thermal equilibrium state at filling υ has a counterpart at filling $1 - \upsilon$, also in equilibrium.

We located the transition temperatures to the charge-ordered states at fillings $\upsilon = 1/7$, $\upsilon = 1/4$, $\upsilon = 1/3$, $\upsilon = 2/5$ and $\upsilon = 1/2$ using standard Monte Carlo sampling of the Gibbs distribution for $\mathcal{H}(n)$ using the Metropolis transition rule. The simulations were performed on a periodic 60×60 hexagonal supercell. To avoid truncation effects, the potential terms $V(r_{ij})$ associated with a site i were replaced by the infinite sum of terms where site j and its occupation is replicated on an infinite hexagonal lattice generated by the supercell. Our transitions maintained υ and were generated by moving a charge to an unoccupied neighbouring site at distance 1 or $\sqrt{3}$. Transition temperatures were determined from the peak in the heat capacity. As our sampling of the temperature in steps of 0.0005 was too coarse to resolve the first-order transitions of the finite (but large) system, the heat capacity peak values in Extended Data Fig. 9 should not be given undue significance. However, the precision of the T_C values given in Extended Data Table 1 should be good to within 0.0005.

Our results are for $d/a = 10$ (close to the experimental value). We also simulated $d/a = 5$ and $d/a = 15$, and found that this changed the T_C values by only a few per cent. All the heat capacity peaks except for $\upsilon = 1/3$ are consistent with first-order transitions. The symmetry breaking in the $\upsilon = 1/3$ state corresponds to the three-state Potts model, which has a continuous transition. Simulations of the stripe phases were made challenging by the high degree of short-range order in the disordered phase. A large number of our local Monte Carlo transitions was required to mix these non-Wigner-crystal-like systems.

From the fact that even the highest transition temperature ($T_C(1/3) = 0.0694$) is numerically small in our energy unit, we learn that the neglected kinetic energy terms in the Hamiltonian would need to be extremely small for the classical model to be valid. We should therefore

not be too concerned that the experimental T_C values of the other fillings, at even lower temperatures, are off the predictions (Extended Data Table 1) based on scaling the model T_C for $\nu = 1/3$.

Data availability

The data that support the plots within this paper, and other findings of this study, are available from the corresponding authors upon reasonable request.

40. Wang, L. et al. One-dimensional electrical contact to a two-dimensional material. *Science* **342**, 614–617 (2013).
41. Chernikov, A. et al. Exciton binding energy and nonhydrogenic Rydberg series in monolayer WS_2. *Phys. Rev. Lett*. **113**, 076802 (2014).
42. Stier, A. V. et al. Magnetooptics of exciton Rydberg states in a monolayer semiconductor. *Phys. Rev. Lett*. **120**, 057405 (2018).
43. He, K. et al. Tightly bound excitons in monolayer WSe_2. *Phys. Rev. Lett*. **113**, 026803 (2014).
44. Efimkin, D. K. & MacDonald, A. H. Many-body theory of trion absorption features in two-dimensional semiconductors. *Phys. Rev. B* **95**, 035417 (2017).
45. Movva, H. C. P. et al. Density-dependent quantum Hall states and Zeeman splitting in monolayer and bilayer WSe_2. *Phys. Rev. Lett*. **118**, 247701 (2017).

Acknowledgements We thank L. Fu for fruitful discussions. Research was primarily supported by the US Department of Energy (DOE), Office of Science, Basic Energy Sciences (BES), under award number DE-SC0019481 (optical spectroscopy and growth of WSe_2 crystals). Device fabrication was supported by US Office of Naval Research under award number N00014-18-1-2368. The growth of the hBN crystals was supported by the Elemental Strategy Initiative of MEXT, Japan and CREST (JPMJCR15F3), JST. K.F.M. also acknowledges support from David and Lucille Packard Fellowship.

Author contributions Y.X. fabricated the devices, performed the measurements and analysed the data. V.E. performed theoretical calculations. S.L., D.A.R. and J.H. grew the bulk WSe_2 crystals, and K.W. and T.T. grew the bulk hBN crystals. Y.X., K.F.M. and J.S. designed the scientific objectives and oversaw the project. Y.X., V.E., K.F.M. and J.S. co-wrote the manuscript. All authors discussed the results and commented on the manuscript.

Competing interests The authors declare no competing interests.

Additional information

Supplementary information is available for this paper at https://doi.org/10.1038/s41586-020-2868-6.

Correspondence and requests for materials should be addressed to Y.X., V.E., K.F.M. or J.S.

Peer review information *Nature* thanks Xiaobo Lu, Fengcheng Wu and the other, anonymous, reviewer(s) for their contribution to the peer review of this work. Peer reviewer reports are available.

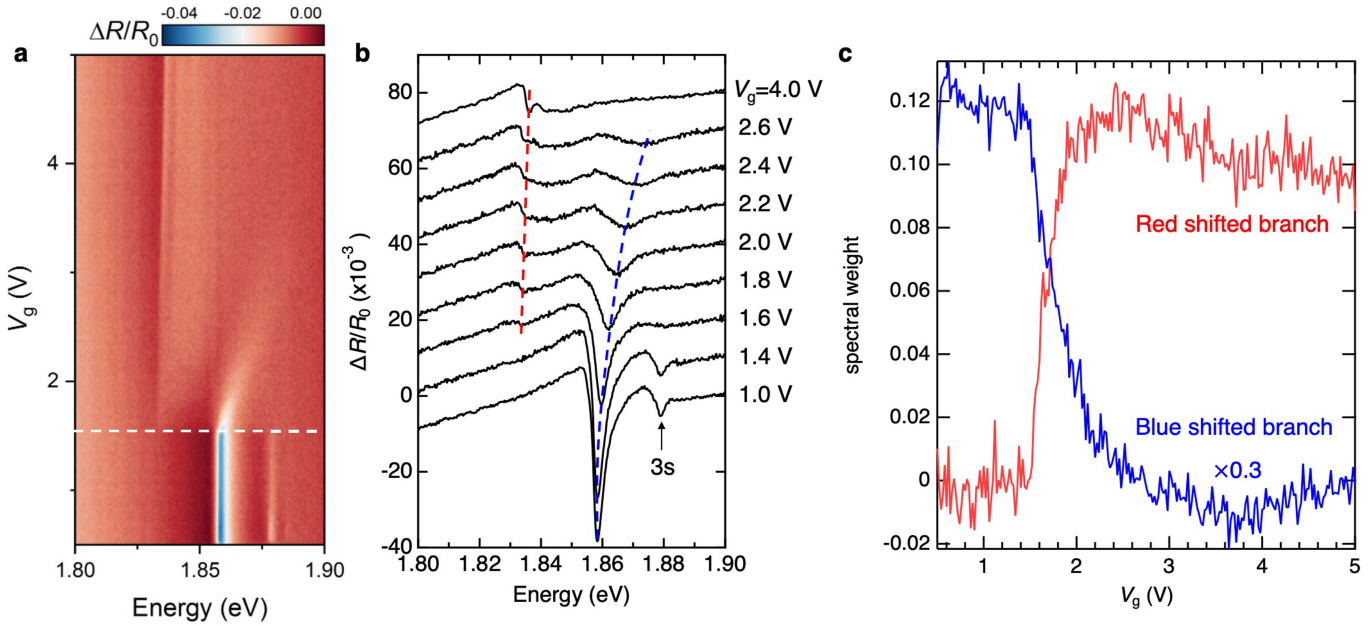

Extended Data Fig. 1 | Additional doping-dependence data and analysis for the control device. a, Gate-dependent reflection contrast ($\Delta R/R_0$) spectrum near the WSe_2 (sensor) 2*s* transition energy (same data as in Fig. 1d, middle). The WS_2 sample is electron-doped above $V_g = 1.5$ V (white dashed line). **b**, Representative linecuts of **a**. Curves are shifted vertically for clarity. The red and blue dashed curves highlight the redshifted and blueshifted branches, respectively. **c**, Spectral weight of the two branches as a function of V_g (calculated after removing the background taken at 1 V and 4 V for the redshifted and blueshifted branches, respectively). The blueshifted branch has been multiplied by a factor of 0.3. The redshifted feature emerges while the blueshifted feature quickly goes to zero at $V_g \approx 1.5$ V.

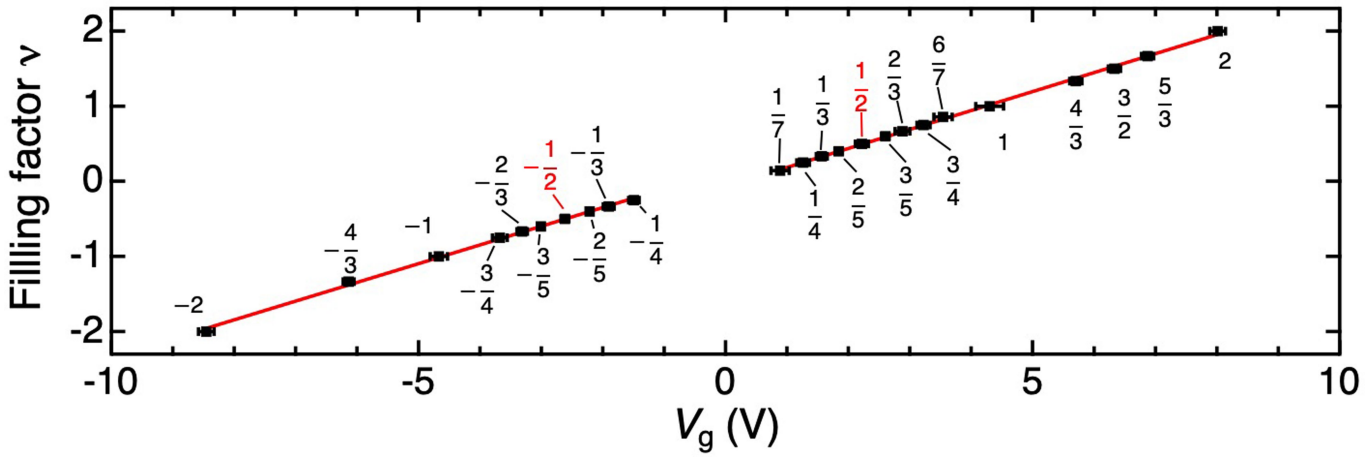

Extended Data Fig. 2 | Assignment of the filling factor of the insulating states. For each insulating state, the position (filled squares) and the FWHM (horizontal bars) in gate voltage are determined through a Lorentzian fit of the 2*s* exciton resonance energy as a function of gate voltage. The red lines are linear fits using four established states $\nu = 2$, $\nu = 1$, $\nu = 2/3$ and $\nu = 1/3$ on the electron and hole sides independently. Both slopes correspond to 0.25 filling per volt. The filling factor of the other states is assigned using the slope as described in Methods.

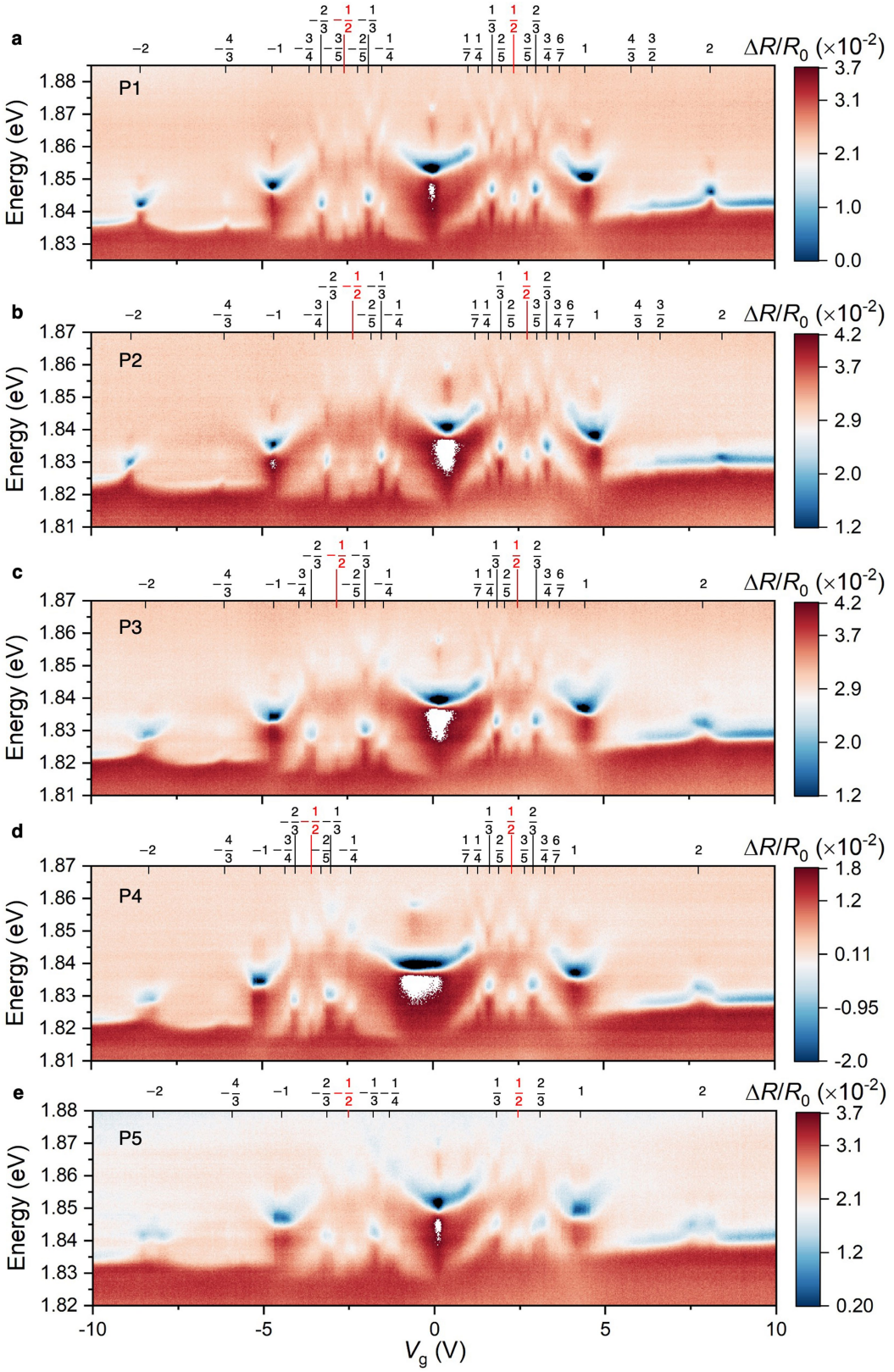

Extended Data Fig. 3 | Results from different regions of the device. **a**–**e**, Gate-dependent reflection contrast spectrum measured at different regions of the device P1 (**a**), P2 (**b**), P3 (**c**), P4 (**d**) and P5 (**e**) at 1.6 K. All share the same *x* axis, given at the bottom. The correlated states that can be identified are labelled on the top axes.

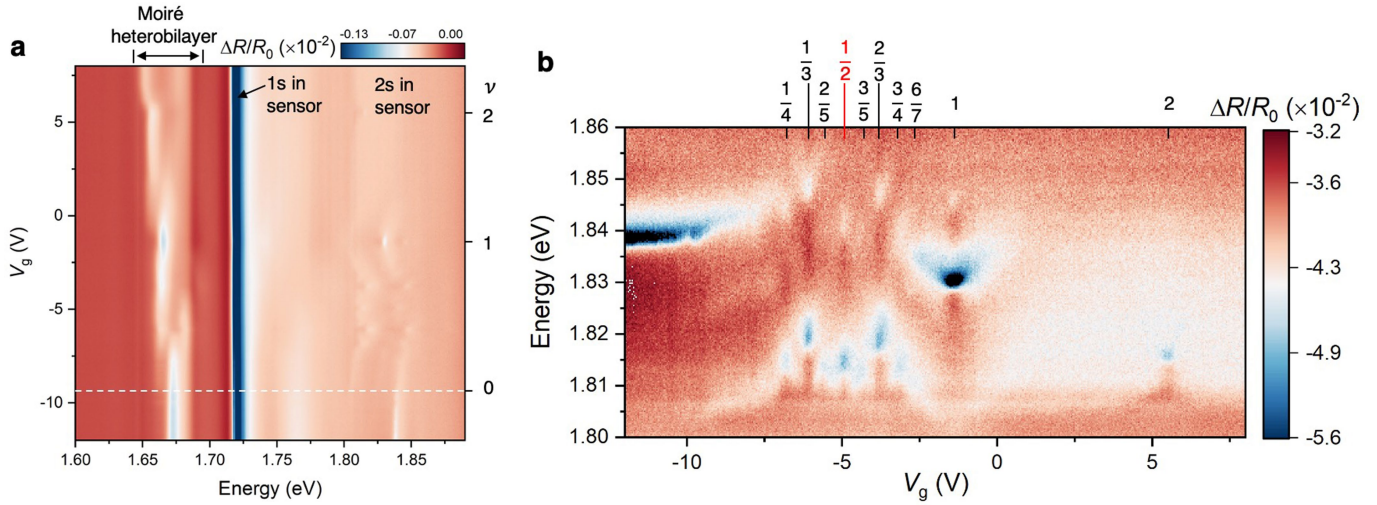

Extended Data Fig. 4 | Results from a different device. a, Gate-dependent reflection contrast spectrum of a different sample as descried in the Methods at 1.6 K. The filling factor is shown on the right axis. A fixed back gate voltage of 8 V is applied to dope the contact region to form good electrical contact between the TMD moiré superlattice and the contact electrode. The top gate voltage V_g is swept to tune the electron doping density. Below $V_g = -9$ V (dashed white line), the sample is charge neutral. **b**, As in **a**, focusing on the 2*s* transition in the sensor. The identified insulating states are marked with their corresponding filling factors.

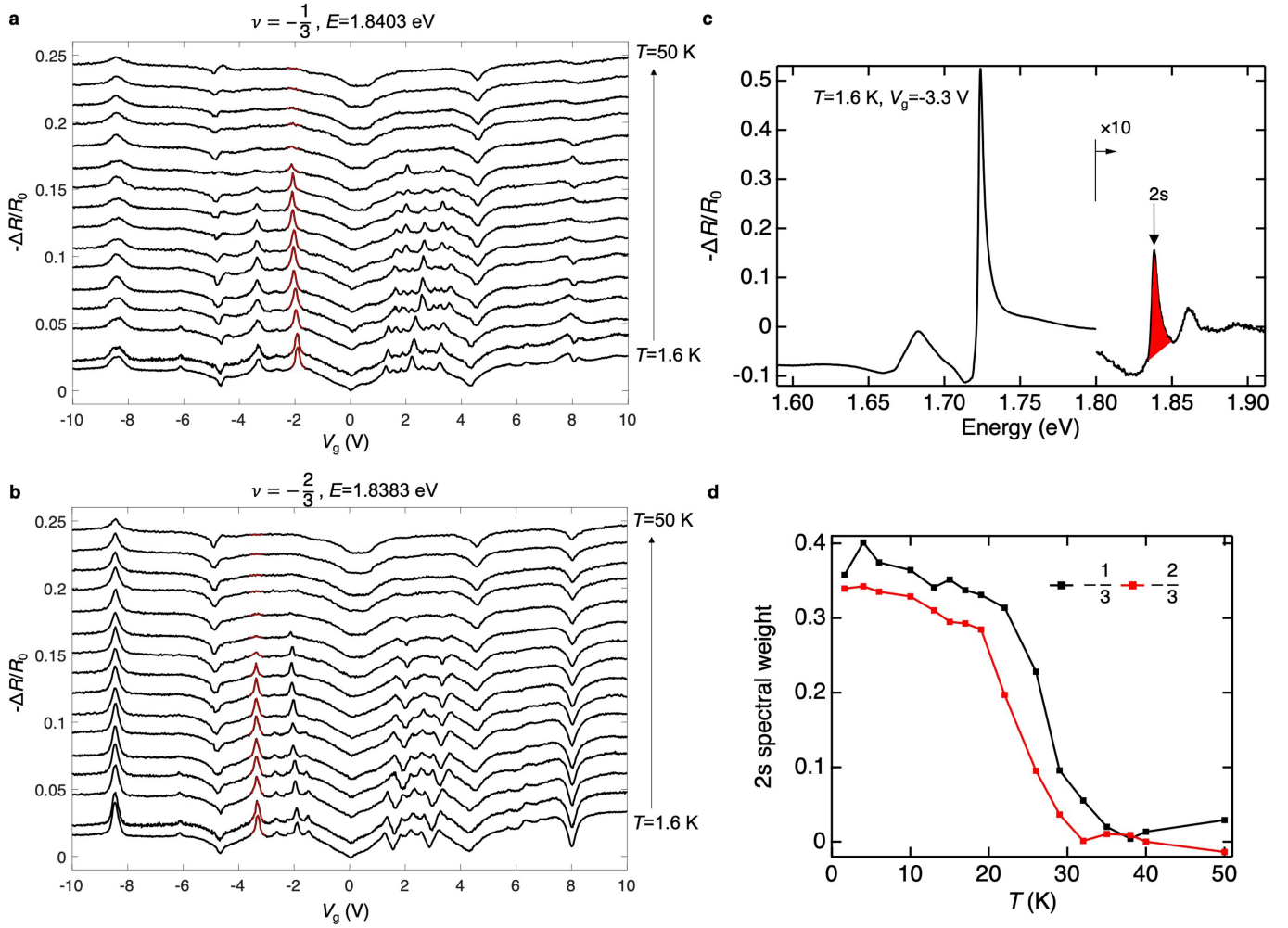

Extended Data Fig. 5 | Analysis of the −1/3 and −2/3 states. a, **b**, Two horizontal line cuts of Fig. 2a at 1.8403 eV (**a**) and 1.8383 eV (**b**). These energies correspond to the 2*s* exciton peak energy for the $\upsilon = -1/3$ and $\upsilon = -2/3$ states, respectively. They appear as peaks in $-\Delta R/R_0$. Results at different temperatures (in ascending order from bottom to top, 1.6 K, 4 K, 6 K, 10 K, 13 K, 15 K, 17 K, 19 K, 22 K, 26 K, 29 K, 32 K, 35 K, 38 K, 40 K and 50 K) are vertically displaced for clarity. The red curves are Lorentzian fits to the peaks for the corresponding states. **c**, Reflection contrast spectrum ($-\Delta R/R_0$) for $V_g = -3.3$ V ($\upsilon = -2/3$) at 1.6 K. The red area underneath the 2*s* peak is integrated to obtain the 2*s* spectral weight. **d**, The 2*s* spectral weight as a function of temperature for state $\upsilon = -1/3$ (black symbols) and $\upsilon = -2/3$ (red symbols). The $\upsilon = -1/3$ state has a slightly higher T_C than the $\upsilon = -2/3$ state. The lines are guides to the eye.

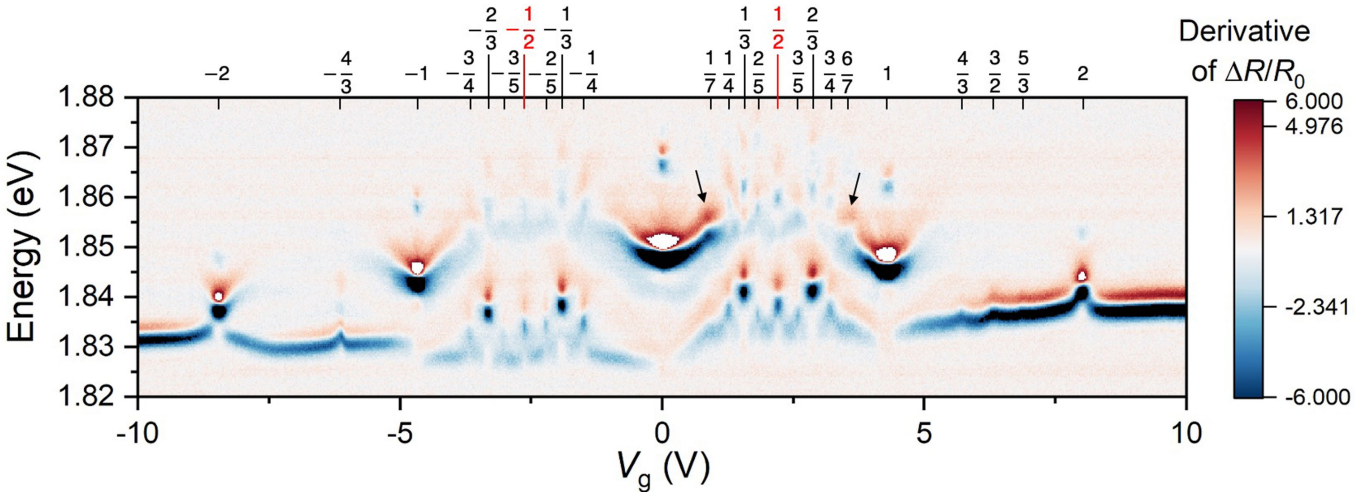

Extended Data Fig. 6 | First derivative of data shown in Fig. 2a with respect to energy. This is used to evaluate the gate voltage and width of the less well-developed insulating states such as those with $|\upsilon| > 1$. The black arrows highlight the enhanced features for the 1/7 and 6/7 states.

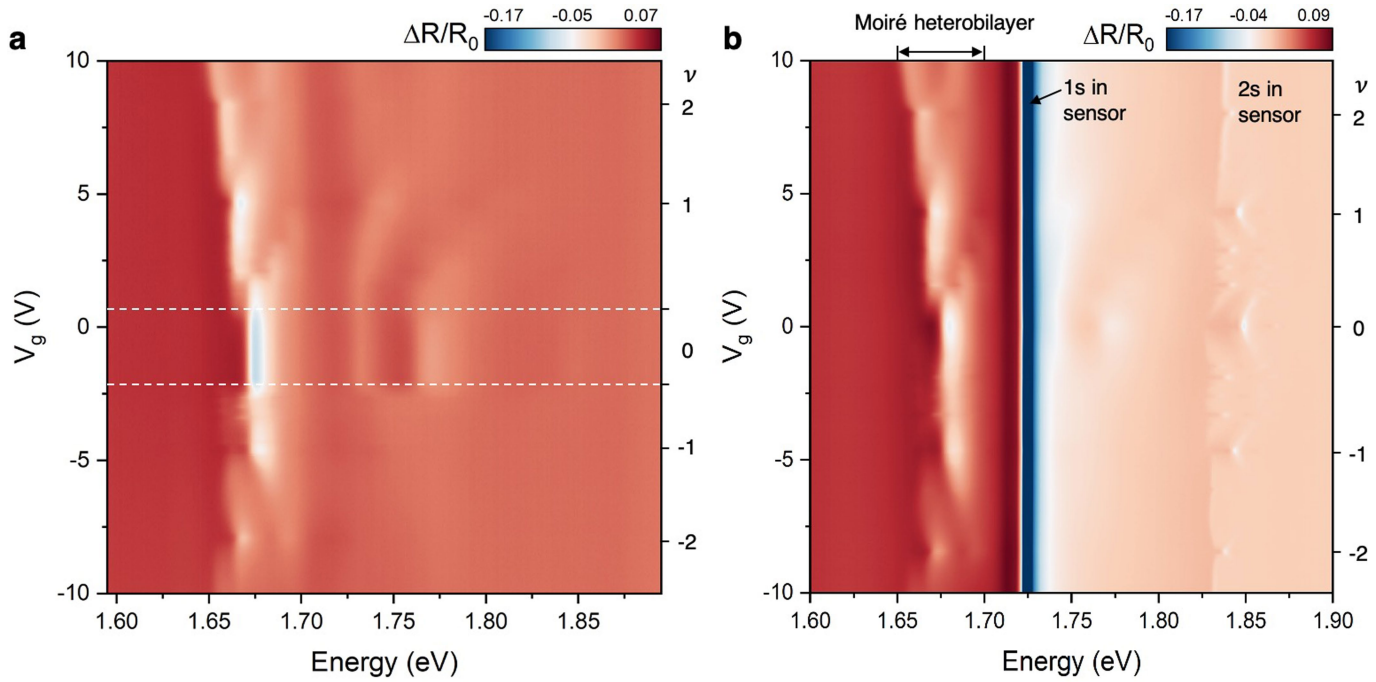

Extended Data Fig. 7 | Optical response of the WSe_2/WS_2 moiré superlattice. a, **b**, Gate-dependent reflection contrast spectrum in regions of the device without (**a**) and with (**b**) the WSe_2 sensor at 1.6 K. The Fermi level is inside the WSe_2/WS_2 bandgap between the dashed lines.

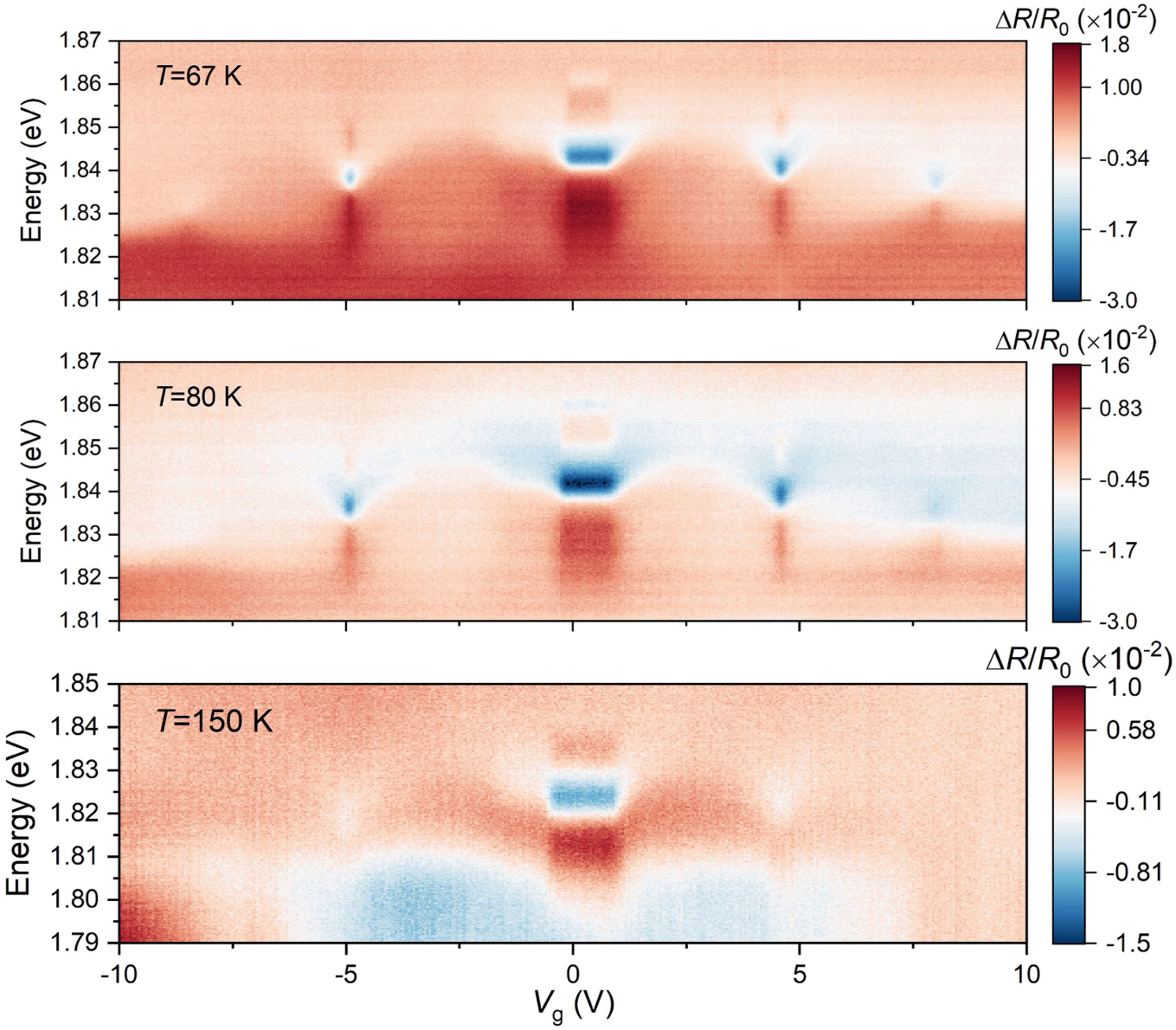

Extended Data Fig. 8 | Contour plots of additional gate-dependent reflection contrast spectrum at higher temperatures. From top to bottom, $T = 67$ K, 80 K and 150 K. All share the same x axis, given at bottom.

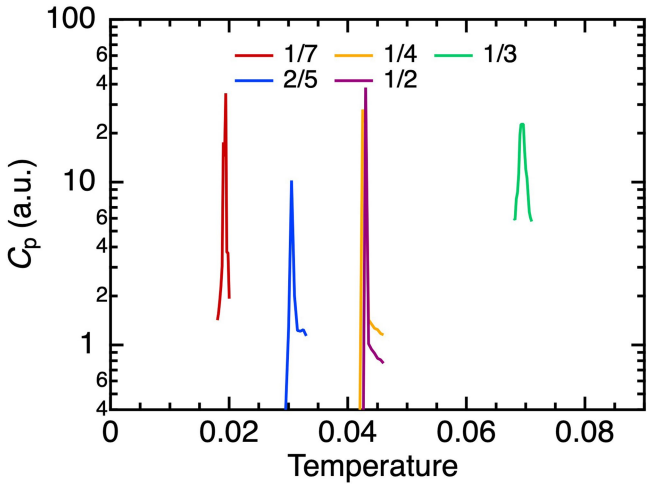

Extended Data Fig. 9 | Transition temperature to the charge-ordered state (simulation). Transition temperatures are determined from the peak in the temperature dependence of the heat capacity C_p for fillings 1/7, 1/4, 1/3, 2/5 and 1/2. Temperature is given in units of the energy $e^2/(4\pi\varepsilon\varepsilon_0 a)$ and d/a is fixed to be 10.

Extended Data Table 1 | Comparison between model and experiment for the transition temperature of the charge-ordered states at fillings $\nu = 1/7, 1/4, 1/3, 2/5$ and $1/2$

	$\nu = 1/7$	$\nu = 1/4$	$\nu = 1/3$	$\nu = 2/5$	$\nu = 1/2$
T_c (model)	0.0194	0.0425	0.0694	0.0305	0.0430
T_c (K, model)	10	23	37	16	23
T_c (K, exp)	10 ± 2	32 ± 2	37 ± 1	18 ± 1	29 ± 2

The model T_C values are in units of the energy $e^2/(4\pi\varepsilon\varepsilon_0 a)$ assuming $d/a = 10$. They are evaluated in kelvins using $\varepsilon = 3.9$, which is chosen to match the highest experimental T_C (at $\nu = 1/3$). The experimental T_C values are taken from the electron doping side. The errors are standard deviations estimated from Fig. 3.